Acta Biochim Biophys Sin xxxx, xx(x): xx-xx
https://cstr.cn/32197.14.abbs.2025238
https://doi.org/10.3724/abbs.2025238
Original Article

Original Article

Genetic mutation and dysfunction of AT2 cells drive B(a)P/LPS-induced inflammation-related lung tumorigenesis: evidence and mechanism of autophagy

Zhihao Tang[1,†], Xianchao Zhou[2,†], Pingping Shang[3], Quanping Yan[3], Ping Lu[1], Yanting Lei[1], Chenfeng Hua[3], Xiaoshan Zhou[4], Qiao Zhang[1], Wei Wang[1], Huaiyong Chen[5], Jian He[2,*], and Feifei Feng[1,*]

[1]College of Public Health, Zhengzhou University, Zhengzhou 45001, China, [2]Center for Single-Cell Omics, School of Public Health, Shanghai Jiao Tong University School of Medicine, Shanghai 200025, China, [3]Zhengzhou Tobacco Research Institute, CNTC, Zhengzhou 450001, China, [4]Department of Laboratory Medicine, Karolinska Institute, Karolinska University Hospital, Stockholm 141 86, Sweden, and [5]Tianjin Key Laboratory of Lung Regenerative Medicine, Haihe Hospital, Tianjin University, Tianjin 300350, China

[†]These authors contributed equally to this work.

*Correspondence address. E-mail: feifeifeng@zzu.edu.cn (F.F.); jih003@sjtu.edu.cn (J.H.)

Received 15 September 2025 Accepted 5 January 2026 Published 9 April 2026

Abstract

The environmental pollutant benzo(a)pyrene (B(a)P), a representative polycyclic aromatic hydrocarbon (PAH), is a recognized carcinogen, and chronic pulmonary inflammation is closely associated with lung carcinogenesis. Although alveolar type 2 (AT2) cells are the origin of lung adenocarcinoma, the genetic and functional changes in AT2 cells and the mechanisms involved in inflammation-related lung tumorigenesis have not been elucidated. Here, C57BL/6J mice are exposed to B(a)P and the inflammatory irritant lipopolysaccharide (LPS) to establish a model of inflammation-related lung tumorigenesis. Single-cell RNA sequencing is performed on lung tissues. DNA mutations in AT2 cells are analyzed via whole-exome sequencing. The protein expression of AT2 cells in lung cancer tissue is determined by immunofluorescence staining. The results reveal that LPS promotes B(a)P-induced lung tumorigenesis; in the whole lungs of B(a)P/LPS, a decreased proportion, altered differentiation trajectory, and increased gene mutation number in AT2 cells are observed. Additionally, in B(a)P/LPS-treated lung cancer tissue, the levels of γ-H2AX DNA damage and the proliferation marker Ki67 in AT2 cells are increased, whereas the levels of differentiation markers are decreased. Single-cell RNA transcriptomics reveals that the autophagy-related genes Foxo3 and Ppp2r5, which are enriched in the PI3K-Akt pathway, and the autophagy-related genes in AT2 cells in lung cancer are decreased in the B(a)P/LPS group. Thus, chronic inflammation promotes DNA damage, gene mutation and dysfunction in AT2 cells, and decreased autophagy in AT2 cells may be an important mechanism for inflammation-related lung tumorigenesis.

Key words inflammation-related lung tumorigenesis, alveolar type 2 cells, autophagy, inflammatory microenvironment, lung cancer, stem cells

Introduction

Benzo(a)pyrene [B(a)P], a typical high-molecular-weight polycyclic aromatic hydrocarbon (PAH), is a highly toxic and carcinogenic pollutant of significant environmental concern [1]. It is ubiquitously present in the environment, particularly in combustion fumes, tobacco smoke, and air pollutants, and primarily enters the human body through the respiratory tract [2,3]. Epidemiological studies indicate that occupational exposure to B(a)P (coke oven workers) is associated with a 3–7 times higher incidence of lung cancer than is the general population [4,5]. Bacterial lipopolysaccharide (LPS), a major component of the outer membrane of gram-negative bacteria, is also widely found in tobacco smoke and in polluted air, such as particulate matter 2.5 ($PM_{2.5}$), where it acts as a carrier [6]. Inhalation of LPS could significantly increase the risk of respiratory

diseases in populations [7,8]. Moreover, LPS-induced inflammation can trigger a robust immune response, leading to prolonged pulmonary inflammation and heightened susceptibility to lung cancer [9]. However, the mechanisms of chronic inflammation-related lung carcinogenesis are poorly defined.

Lung cancer is the first malignant cancer with the highest mortality and mobility [10]. Lung adenocarcinoma (LUAD), accounting for approximately 60% of newly diagnosed lung cancer cases, is the most common lung cancer subtype and is characterized by rapid growth and poor patient outcomes [11]. LUAD is closely related to environmental pollutants, such as tobacco smoke [12], coke oven emissions [13] or smog [14], which induce injury or/and mutation of the cells in the lung, especially epithelial cells [15]. Furthermore, chronic inflammation is widely believed to play a significant role in the occurrence of LUAD [16]. Our research group reported that LPS-induced chronic inflammation could promote B(a)P-induced lung carcinogenesis, and 87.5% of these cases involved lung adenocarcinoma [17].

LUAD mainly arises from alveolar type 2 (AT2) cells [18,19], which function as alveolar stem cells by self-renewing, self-repairing and replacing AT1 cells [20]. Studies have reported that exogenous chemicals can affect AT2 cells and induce the occurrence of LUAD. For example, smoking can promote the differentiation of AT2 cells into AT2-like cells and ultimately drive lung adenocarcinoma tumorigenesis [12]. Long-term tobacco smoke exposure leads to an imbalance in the proliferation and differentiation of AT2 cells through epigenetic dysregulation of the IGF2-Wnt signaling pathway and induces the occurrence of LUAD [21]. However, how environmental pollutants such as B(a)P, in combination with chronic inflammatory stimuli such as LPS, impact the function, genomic stability, and transformation potential of AT2 cells remains poorly understood.

Autophagy plays a critical role in tumorigenesis and is a crucial biological process in which cells degrade damaged or redundant components through the lysosomal system [22]. This core mechanism is essential for the recycling of cellular components and the maintenance of cellular homeostasis [23]. Autophagy dysregulation is closely associated with lung tumorigenesis [24]. In addition, autophagy and inflammation are dynamically and bidirectionally regulated. On the one hand, autophagy alleviates chronic inflammation by clearing inflammatory mediators and dampening excessive inflammatory reactions [25]. On the other hand, inflammatory cytokines such as TNF-α and IL-1β regulate autophagy [26,27]. In chronic pulmonary inflammatory environments, persistent inefficient autophagy is associated with lung injury, leading to pulmonary diseases [28]. Autophagy deficiency in AT2 cells disrupts cellular function, ultimately driving pulmonary fibrosis [29]. However, whether impaired autophagy in AT2 cells represents a mechanistic link between pollutant exposure, inflammation, and tumorigenesis has not been previously investigated.

In this study, we constructed a mouse model of inflammation-related lung tumorigenesis via B(a)P combined with LPS, which was created by our research group [30]. Using single-cell RNA sequencing and whole-exome DNA sequencing, we profiled the transcriptional changes, DNA mutations, and autophagy status of AT2 cells in this model. Our findings reveal that chronic inflammation aggravates B(a)P-induced lung cancer via increased DNA damage, gene mutations, impaired differentiation, and suppressed autophagy in AT2 cells, offering novel insights into how environmental pollutants and inflammation synergize to drive lung carcinogenesis.

Materials and Methods

Mice

C57BL/6J mice (6–8 weeks and 19–23 g), with an equal distribution of males and females totaling 120, were procured from Beijing Vital River Company (Beijing, China). They were housed in an SPF-level animal facility at the School of Public Health, Zhengzhou University, with a 12-h light-dark cycle, suitable temperature and humidity, and 4 mice per cage. The mice were provided with ample sterile feed and sterilized water, and their bedding was autoclaved regularly. Following a two-week acclimation period in the animal facility, the mice were randomly assigned to experimental groups, and subsequent experiments were conducted. The entire animal study was conducted in compliance with the guidelines and approved by the Experimental Animal Ethics Committee of Zhengzhou University (approval No. ZZUIRB2023-144).

Model establishment

C57BL/6J SPF experimental mice were randomly divided into four groups: (1) control group; (2) LPS group; (3) B(a)P group, and (4) B(a)P/LPS group. Tracheal instillation was performed on the experimental mice, with each mouse receiving a 50-μL volume of instillation solution. B(a)P and LPS from *Escherichia coli* were purchased from (Sigma-Aldrich, St Louis, USA). The concentration of B(a)P was 20 mg/mL, and the concentration of LPS was 0.05 mg/mL. The B(a)P group and B(a)P/LPS group received tracheal instillation of B(a)P once a week for 4 consecutive weeks. The control group received the same volume of solvent. The first exposure to B(a)P was designated week 0. The B(a)P/LPS group and LPS group began tracheal instillation of LPS at week 6, which was administered once every 3 weeks for a total of 5 times. After the exposure period, the mice were maintained under normal conditions until week 34, at which point they were sacrificed [30].

Lung organ coefficient

After the lungs were isolated from the mice, the surface fat and fascia were removed to ensure consistent surface treatment of all the mouse lungs. Blotting paper was used to absorb the surface liquid of the lungs. The lungs were weighed via an electronic balance, and the organ coefficient was calculated. Lung weight and mouse body weight were measured in grams. Organ coefficient = (organ weight/mouse body weight after anesthesia) × 100%.

Hematoxylin-eosin staining

Staining was performed via a hematoxylin-eosin (H&E) staining kit (Servicebio, Wuhan, China). The left lung, which was stored in formaldehyde (Servicebio), was paraffin-embedded, sectioned, and deparaffinized. Sections were then stained with hematoxylin-eosin, dehydrated, and mounted with neutral resin. Images were captured and analyzed via an advanced microscope (LX71; Olympus, Tokyo, Japan).

Single-cell RNA-seq and data analysis

Lung tissues were pooled for single-cell sequencing. Single-cell transcriptome sequencing was performed via the 10× Genomics platform, which is outsourced to Singleron (Nanjing, China). The

tissue samples were dissociated into single-cell suspensions using sCelLiVE™ tissue dissociation solution and injected into SCOPE-chip™ microfluidic chips. Beads with unique cell barcodes were added to the chip wells, ensuring that each well contained only one bead. Following cell lysis, beads with specific cell barcodes and unique molecular identifiers (UMIs) capture mRNA by binding to poly(A) tails. The beads were then collected from the chip, and the captured mRNA was reverse transcribed into cDNA and amplified. The cDNA was subsequently fragmented, ligated with adapters, and constructed into a library. After quality control, the cDNA library was sequenced on an Illumina sequencer, and the resulting data were analyzed.

Single-cell RNA sequencing data were analyzed via RStudio (version 4.3.0) in R, which employs the Seurat package and related tools for comprehensive analysis and exploration. Cells whose mitochondrial gene content was less than 20% and whose gene counts were between 200 and 4000 per cell were selected for further analysis. The NormalizeData function was used to normalize the data, and the FindVariableFeatures function identified highly variable genes. Dimensionality reduction was performed via the t-SNE and UMAP methods. Cells were clustered via the FindClusters function. Functional analysis and pathway enrichment analysis were conducted via the clusterProfiler [31], DOSE [32], and ComplexHeatmap [33] packages to perform Gene Ontology (GO) and Kyoto Encyclopedia of Genes and Genomes (KEGG) pathway analyses. In analysis of cell-cell communication, we employed the CellChat packages to map the cell-cell communication network.

Flow cytometry sorting

After mice were injected with sodium pentobarbital, they were incubated, and their lungs were excised. The lungs were perfused with 4 U/mL elastase (Worthington Biochemical Corporation, Lakewood, USA). After digestion, the lung tissue was placed in a culture dish and minced into a slurry with a blade. DNAse (Sigma-Aldrich) was added to each dish and incubated at 37°C for 15 min. 10 mL of HBSS+ medium was added to the dish to terminate the reaction, and the mixture was triturated, the HBSS+ solution was prepared by adding 10 mL of FBS (Lonsera, Jersey City, USA), 5 mL of HEPES (Sigma-Aldrich), and 5 mL of PS (Gibco, Carlsbad, USA) to 500 mL of HBSS (Solarbio, Beijing, China) solution. The cell suspension was then filtered through a 70-μm mesh (Falcon; BD Biosciences, San Jose, USA) and collected in a new 50-mL centrifuge tube. The mesh was ground and washed with 10 mL of HBSS+ medium. RBC lysing buffer (Thermo Fisher Scientific, Wilmington, USA) was added to resuspend the cells and incubated for 90 seconds. Then, 20 mL of HBSS+ was added to terminate the reaction. Primary antibodies against CD24, CD326, SCA-1, CD31, CD34, CD45, and CD24 were added to the sample tubes and incubated at 4°C in the dark for 45 min. Secondary antibodies were then added and incubated at 4°C in the dark for 30 min. All antibodies were purchased from Invitrogen (Carlsbad, USA). The cells were sorted using a BD-FACSAriaIII flow cytometer (BD Biosciences).

Immunofluorescence double staining

The paraffin-embedded lung tissue sections (4 μm) were placed in antigen retrieval solution and subjected to high-pressure retrieval for 2 min, followed by blocking with BSA (10% donkey serum, goat-derived primary antibody). The sections were then stained with the following diluted primary antibodies: rabbit anti-SPC (1:200; Proteintech, Wuhan, China), rabbit anti-γ-H2AX (1:200; BIOSS, Beijing, China), rabbit anti-p-Akt (1:200; Proteintech), rabbit anti-Foxo3 (1:500; Proteintech), rabbit anti-Ki67 (1:200; Invitrogen), and rabbit anti-Pdpn (1:200; Invitrogen). The sections were incubated with Alexa Fluor 488/594-conjugated secondary antibodies (1:200; Servicebio) at room temperature in the dark for 50 min, followed by incubation with diluted DAPI staining solution at room temperature for 10 min. The sections were then mounted with anti-fade mounting medium and scanned via an advanced fluorescence microscope (ECLIPSE C1; Nikon, Tokyo, Japan) at different excitation wavelengths.

DNA whole-exome sequencing

Samples were transferred to centrifuge tubes, and cell lysis was performed. Protease digestion was performed to remove proteins from the samples. The clean gDNA solution was transferred to new centrifuge tubes, and a NanoDrop 2000 spectrophotometer (Thermo Fisher Scientific) was used to measure the quality and concentration of the extracted gDNA. The fragmented DNA was subjected to end repair, tailing, adapter ligation, and amplification to construct the gDNA library. The prepared gDNA library was hybridized with specific probes to capture targeted regions, followed by PCR amplification and indexing to obtain the exome library. Quality checks were performed on the constructed library, which was then loaded onto a sequencer. The sequencer performed PE150 mode sequencing (NovaSeq 6000; Illumina, SanDiego, USA) on the DNA fragments in the library (NovaSeq 6000s; Illumina). The quality-controlled sequencing data were aligned with the reference genome or other relevant sequences, and the genomic features of the samples were interpreted on the basis of the analysis results.

Quantitative RT-qPCR

Total RNA was extracted from the sorted cells via TRIzol (Thermo Fisher Scientific) according to the manufacturer's instructions. cDNA was synthesized via reverse transcription via SuperMix II (Vazyme Biotech, Nanjing, China), and RT-qPCR was performed on a Fast Real-time PCR System (Applied Biosystems, Foster City, USA). The following primers were used: *β-actin* (forward primer 5′-GGCCAACCGTGAAAAGATGA-3′ and reverse primer 5′-CAGCCTG GATGGCTACGTACA-3′), *Ppp2r5a* (forward primer 5′-GCCAAT TATGTTTGCCAGTTTG-3′ and reverse primer 5′-CGAAAAGCTTGC CATTCATTTC-3′), *Foxo3* (forward primer 5′-CGCTGTGT GCCCTACTTC-3′ and reverse primer 5′-CGCTGTGTGCCCTAC TTC-3′), Lc3b (forward primer 5′-AAGCCTTCTTCCTCCTGGTGAA TG-3′ and reverse primer 5′-ATTGCTGTCCCGAATGTCTCCT G-3′), *Atg5* (forward primer 5′-TGAAAGAGAAGCAGAACCA TACT-3′ and reverse primer 5′-GGGTGTGCCTTCATATTCAAAC-3′), *Ki67* (forward primer 5′-AACTTGCCTCCTAATACACCACTG-3′ and reverse primer 5′-GCCGTTCCTTGATGATTGTCTTG-3′), *Pdpn* (forward primer 5′-ATCTACTGGCAAGGCACCTCTG-3′ and reverse primer 5′-GTGGTTGTACTCTCGTGTTCTCTG-3′). All the primers used in the experiments were designed and synthesized by Sangon Biotech (Shanghai, China).

Statistical analysis

Statistical analysis was performed using SPSS 25.0, and data were visualized with GraphPad Prism 9. Results are presented as the mean ± SD. One-way ANOVA was applied for multiple group

comparisons, with Bonferroni's test used for subsequent pairwise analyses. The significance level was set at $\alpha = 0.05$.

Results

B(a) P/LPS exacerbates the occurrence of lung tumors

There were no lung tumors observed in the control or LPS groups, while lung tumors were visible in the B(a)P and B(a)P/LPS groups (Figure 1A). The lung coefficient of the mice in the B(a)P/LPS group differed significantly from that in the LPS group ($P < 0.05$) (Figure 1B). Pathological results revealed no tumor formation in the control and LPS groups, with thickening observed in the airway and alveolar regions of the LPS group. Pathological tumors were observed in both the B(a)P/LPS and B(a)P groups, with more pronounced pathological changes in the B(a)P/LPS group than in the B(a)P group (Figure 1C). Similarly, compared with the tumorigenesis rate of 33.33% in the B(a)P group, the tumorigenesis rate in the B(a)P/LPS group was 62.5% (Table 1). In conclusion, B(a)P and B(a)P/LPS induced lung tumorigenesis in mice, and B(a)P/LPS exacerbated lung tumorigenesis.

Single-cell RNA-seq reveals the response of AT2 cells to inflammation-related lung tumorigenesis

To explore the molecular mechanisms underlying B(a)P/LPS-induced inflammation-related lung tumorigenesis, we performed single-cell RNA-seq on lung tissues collected from control, B(a)P and B(a)P/LPS mice (Figure 2A). On the basis of the expression of marker genes in different cell clusters, the clusters were annotated according to known marker genes in lung tissue, resulting in 13 identified cell clusters after classification by specific genes (Figure 2E). Further analysis of the total cell populations in the three lung tissue groups revealed significant changes in the proportions of B-cell clusters, endothelial cells and lung epithelial cell clusters. Compared with that in the control group, the proportion of B-cell clusters in the B(a)P group was 46.78%, which decreased to 16.03% in the B(a)P/LPS group. Conversely, the percentage of endothelial cells increased from 21.77% in the B(a)P group to 41.26% in the B(a)P/LPS group, and the percentage of lung epithelial cell clusters increased from 26.24% in the B(a)P group to 47.91% in the B(a)P/LPS group (Figure 2B).

On the basis of these results, lung epithelial cells are the primary source cells of lung tumors. Further subpopulation analysis was conducted on the lung epithelial cell clusters. The subpopulations

Table 1. Tumorigenesis rate in the lungs of mice

Group	N_{Total}	N_{Tumor}	Weight (g)	Tumorigenesis rate
Control	16	0	23.75±3.09	0
LPS	19	0	25.24±3.41	0
B(a)P	18	6	25.74±2.92	33.33%*
B(a)P/LPS	24	15	26.64±3.43	62.5%*#

N_{Total}: number of mice; N_{Tumor}: number of mice with tumor occurrence. *$P < 0.05$ vs control; #$P < 0.05$ vs B(a)P.

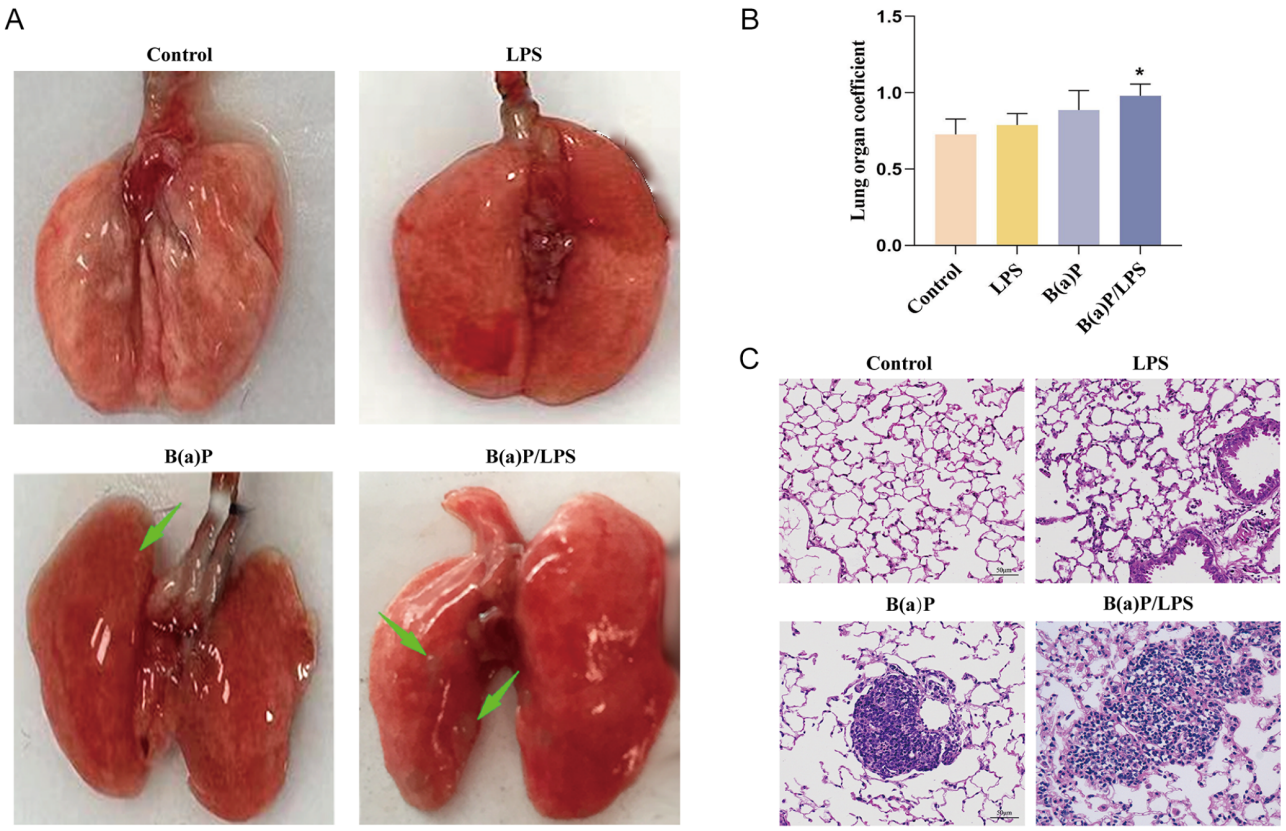

Figure 1. B(a)P/LPS exacerbates the occurrence of lung tumor (A) Lung tumors were observed in both the B(a)P/LPS group and the B(a)P group. (B) Changes in lung coefficient during the occurrence of inflammation-related lung tumorigenesis in mice. (C) Histopathological examination of mice lung tissues with HE staining (scale bar: 50 μm). *$P < 0.05$ vs LPS.

were annotated according to the expression levels of the markers in each subcluster, resulting in the identification of five distinct cell types: club cells, AT2 cells, ciliated cells, AT1 cells, and goblet cells. Visualization of the subpopulations through t-SNE nonlinear dimensionality reduction revealed consistent cell distributions across groups, with noticeable differences in cell counts (Figure 2C,F). Among the subpopulations of lung epithelial cells, AT2 cells accounted for 31.8% of the total cell count in the B(a)P group and 21.4% in the B(a)P/LPS group, both of which were lower than those in the control group (Figure 2D). Furthermore, cell-cell communication analysis revealed a significant decrease in signaling interactions between AT2 cells and alveolar neutrophils in the B(a)P/LPS group compared with the B(a)P group (Figure 2G,H). Together, compared with that in the B(a)P group, the proportion of AT2 cells in B(a)P/LPS-induced inflammation-related lung tumorigenesis in mice was lower.

Altered differentiation trajectory and differential gene expression of AT2 cells in inflammation-related lung tumorigenesis

Subsequently, pseudotime analysis was conducted on the epithelial cell populations in both groups, revealing altered differentiation trajectories in the lung epithelial cells. Lung epithelial cells exhibited five differentiation states in the B(a)P group but six differentiation states in the B(a)P/LPS group. Compared with that in the B(a)P group, a reduction in AT2 cells during the early stage was observed, while many AT2 cells were present in the intermediate stage in the B(a)P/LPS group (Figure 3A). These findings suggest that the differentiation trajectory of AT2 cells is altered during inflammation-related lung tumorigenesis induced by B(a)P/LPS.

GO and KEGG enrichment analyses were conducted on the differentially expressed genes (DEGs) in AT2 cells between the B(a)

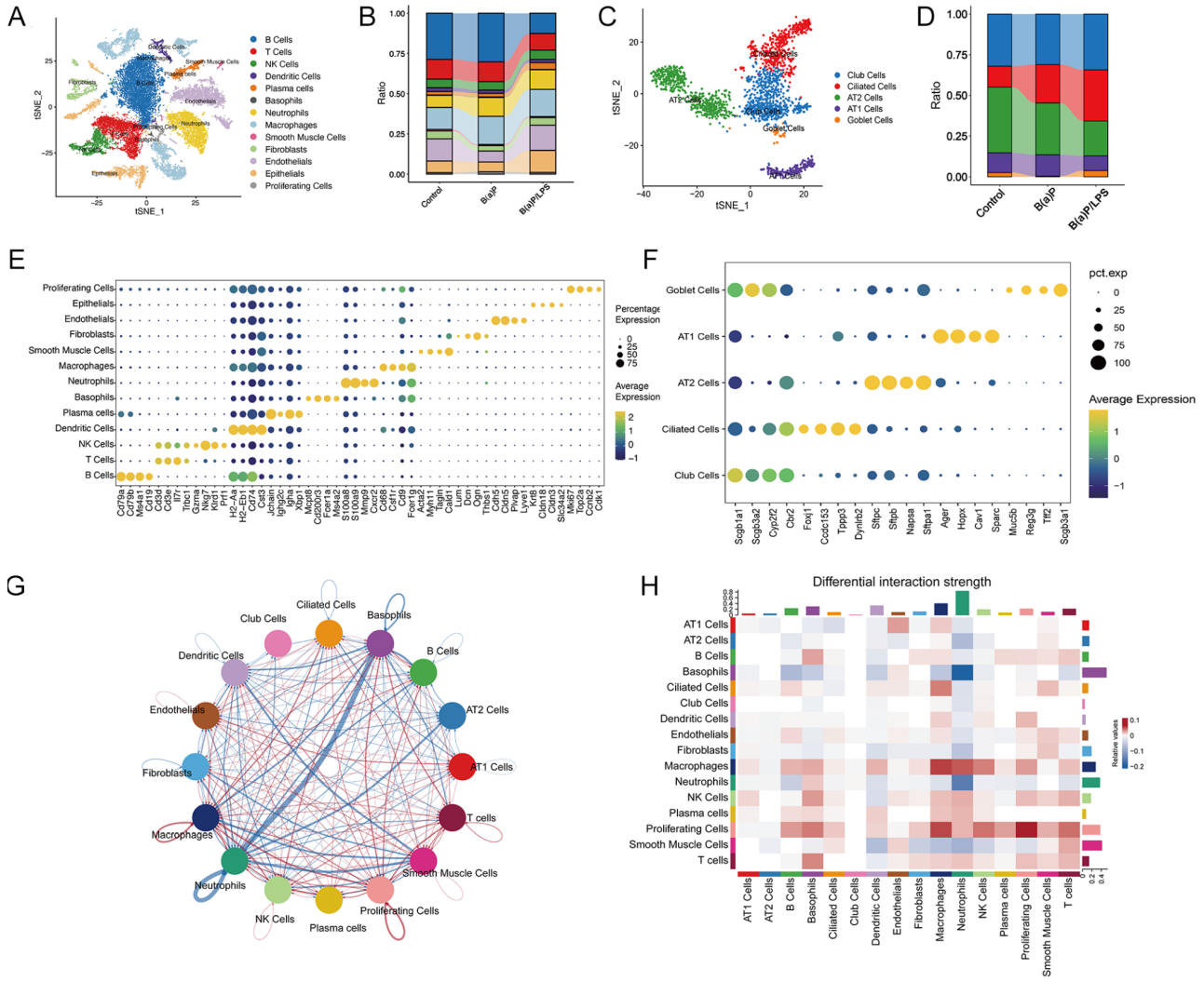

Figure 2. Single-cell RNA-seq reveals responses of AT2 cells in inflammation-related lung tumorigenesis (A) The t-SNE visualization plot annotated with marker genes. (B) The proportion of each cell cluster annotated in mice lung tissue after clustering. (C) The t-SNE plot of lung epithelial cell subpopulations after clustering annotation. (D) The proportion of subpopulations of lung epithelial cells within their respective clusters. (E) The Dot Plot displaying the gene expression signatures of the marker genes corresponding to each cell type within lung tissues. (F) The Dot Plot displaying the gene expression signatures of the marker genes corresponding to each cell type within lung epithelial cell clusters. (G,H) Cell-cell communication between cells between the B(a)P and B(a)P/LPS groups.

P/LPS group and the B(a)P group. The FindMarkers function was used to identify DEGs, revealing 348 DEGs between the two groups, with 263 genes downregulated and 85 genes upregulated. GO analysis indicated that the DEGs were involved primarily in biological processes such as autophagy and processes utilizing autophagic mechanisms. The cellular components were associated mainly with the ribosome and proteasome complex, while the molecular functions included ubiquitin protein ligase binding and

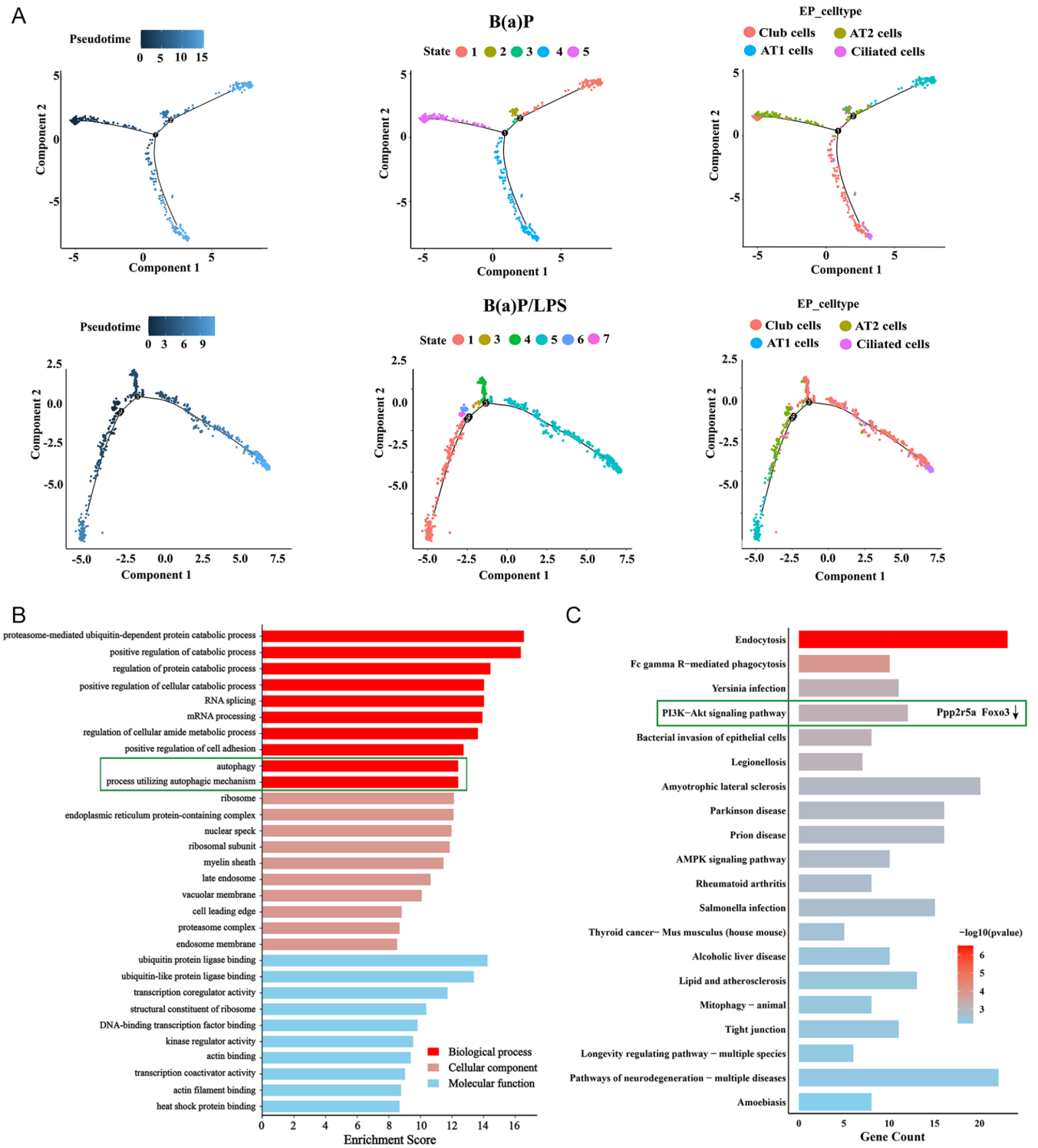

Figure 3. Altered differentiation trajectory and differential gene expression analysis of AT2 cells in inflammation-related lung tumorigenesis (A) Pseudotime analysis of epithelial cell clusters in the B(a)P/LPS group and the B(a)P group revealed alterations in the differentiation trajectories of lung epithelial cell clusters in both groups. (B) GO analysis of differential genes in AT2 cells between the B(a)P/LPS group and the B(a)P group. (C) KEGG pathway enrichment analysis of differential genes in AT2 cells between the B(a)P/LPS group and the B(a)P group.

transcription coregulator activity (Figure 3B). KEGG pathway enrichment analysis of enriched genes revealed that the DEGs were enriched in pathways such as FcγR-mediated phagocytosis, the PI3K-Akt signaling pathway, the AMPK signaling pathway, and mitophagy (Figure 3C). Further analysis of these signaling pathways revealed that the Ppp2r5a and Foxo3 genes were significantly downregulated in the PI3K/Akt signaling pathway.

DNA damage and genetic mutations in AT2 cells in inflammation-related lung tumorigenesis

To assess functional and genetic changes in AT2 cells during inflammation-related lung tumorigenesis, flow cytometry was used to sort AT2 cells from fresh lung tissue. CD326$^+$ cells (lung epithelial cells) and AT2 cells (CD31$^-$CD34$^-$CD45$^-$CD326$^+$CD24$^-$Sca-1$^-$) were identified (Supplementary Figure S1). AT2 cells were selected on the basis of these marker antibodies. To investigate DNA damage in AT2 cells during inflammation-related lung tumorigenesis, immunofluorescence colocalization of the AT2 cell marker SPC and the DNA damage marker γ-H2AX was performed on mouse lung cancer tissue. The number of colocalized cells was greater in the B(a)P/LPS group than in the B(a)P group (Figure 4A–C). Compared with those in the B(a)P group, the levels of the DNA damage marker γ-H2AX were significantly elevated in the B(a)P/LPS group. The elevation of γ-H2AX levels in AT2 cells during inflammation-related lung tumorigenesis suggested that inflammation may exacerbate DNA damage in AT2 cells.

DNA whole-exome sequencing was subsequently performed on AT2 cells from the control, B(a)P, and B(a)P/LPS groups, with the sequencing results corrected for background values from the control group. The DNA mutations in both the B(a)P and B(a)P/LPS groups were classified into five types, with missense mutations being the most prevalent. Single-nucleotide variant analysis revealed that thymine (T) and cytosine (C) were relatively unstable and prone to mutations (Figure 4D). Furthermore, the number of DNA mutations differed between the B(a)P and B(a)P/LPS groups. Analysis of these mutated genes revealed that 12 mutated DNA sequences (Table 2) in the B(a)P group were associated with tumorigenesis. In the B(a)P/LPS group, 16 mutated DNA sequences were linked to tumor occurrence (*e.g.*, Rasal3, Tnfsf14 and Map3k4) (Table 3). Notably, compared with that in the B(a)P group, the number of mutated genes increased significantly in the B(a)P/LPS group.

Functional abnormalities of AT2 cells in mice with inflammation-related lung tumorigenesis

Compared with the B(a)P group, the B(a)P/LPS group presented increased expression of the proliferation marker gene Ki67 in AT2 cells (Figure 5A). Immunofluorescence double staining was used to detect the expression of the proliferation marker protein Ki67 in AT2 cells in the lung tissues of different groups. The number of cells with red cytoplasm and blue nuclei after merging was observed. Additionally, Ki67 expression was greater in the B(a)P/LPS group than in the B(a)P group (Figure 5B–D).

To validate the changes in AT2 cell differentiation during inflammation-related lung tumorigenesis, we measured the relative expression of the AT2 cell differentiation marker gene *Pdpn*, which is a protein marker of AT1 cells. Compared with that in the B(a)P group, the relative expression of Pdpn was lower in the AT2 cells of the B(a)P/LPS group (Figure 5E). To further verify the changes in the differentiation capacity of AT2 cells in inflammation-related lung tumorigenesis, immunofluorescence double staining was performed to detect the expression of the differentiation marker protein Pdpn in AT2 cells. The results indicated that, compared with that in the B(a)P group, the protein expression of Pdpn was relatively lower in the B(a)P/LPS group (Figure 5F–G).

Autophagy in AT2 cells is reduced in mice with inflammation-related lung tumorigenesis

Single-cell RNA sequencing analysis revealed DEGs, including the autophagy-related genes *Foxo3* and *Ppp2r5a*, in AT2 cells in the B(a)P/LPS group compared with those in the B(a)P group, and the *Foxo3* and *Ppp2r5a* genes were enriched in the PI3K-Akt pathway. The decreased expression of the autophagy-related genes *Foxo3*, *Ppp2r5a*, *Lc3b*, and *Atg5* was verified in AT2 cells in the B(a)P/LPS group by qRT-PCR (Figure 6C–F). Additionally, the protein level of p-Akt was increased (Figure 6A), whereas the protein level of Foxo3 was decreased (Figure 6B) in AT2 cells in the lung cancer tissues of mice exposed to B(a)P/LPS, as shown by immunofluorescence double staining.

Discussion

In this study, we successfully established a mouse model of inflammation-related lung tumorigenesis by B(a)P/LPS and found that: (1) LPS promoted B(a)P-induced lung tumorigenesis; in the whole lungs of the mice in the B(a)P/LPS group, the proportion of AT2 cells decreased, the differentiation trajectory of AT2 cells was altered, and the number of gene mutations in AT2 cells increased. (2) The levels of DNA damage and proliferation markers in AT2 cells were increased, and the levels of differentiation markers were decreased in AT2 cells in the lung cancer tissues of mice exposed to B(a)P/LPS. (3) The expression of autophagy-related markers in AT2 cells in mouse lung cancer was decreased in the B(a)P/LPS group.

Lung epithelial stem cells play a complex and crucial role in the occurrence of lung cancer [34]. AT2 cells are a type of lung epithelial stem cell and are reported as the origin cells of LUAD [[29]. In this study, single-cell RNA sequencing of mouse lung tissue revealed that the proportion of AT2 cells was lower in the B(a)P and B(a)P/LPS groups than in the vehicle control group. We speculated that in the whole lung, there were normal and abnormal (perhaps malignant transformation) AT2 cells and that normal AT2 cells were damaged too severely to proliferate for repair. In the whole lung, the proportion of AT2 cells was lower in the B(a)P/LPS group than in the B(a)P group. The reason may be that the chronic inflammation induced by LPS promotes a decrease in the proportion of normal AT2 cells during B(a)P-induced lung tumorigenesis. A study demonstrated that persistent inflammation following hepatitis virus infection led to the death of normal hepatocytes or replacement by cancerous cells, resulting in a decrease in the proportion of hepatocytes [35]. The expression of the proliferation marker Ki67 in AT2 cells was increased in lung cancer tissue from mice in the B(a)P and B(a)P/LPS groups compared with that in the vehicle control group. It is speculated that most AT2 cells in lung cancer tissue undergo malignant transformation and proliferate quickly and become neoplastic. Additionally, the expression of the proliferation marker Ki67 in AT2 cells was upregulated in lung cancer tissue in the B(a)P/LPS group compared with that in the B(a)P group, which may be related to persistent inflammation promoting the proliferation of cancer cells [36]. Although the expression of the proliferation marker Ki67 in AT2 cells in lung cancer tissue was increased and the proportion of AT2 cells in the

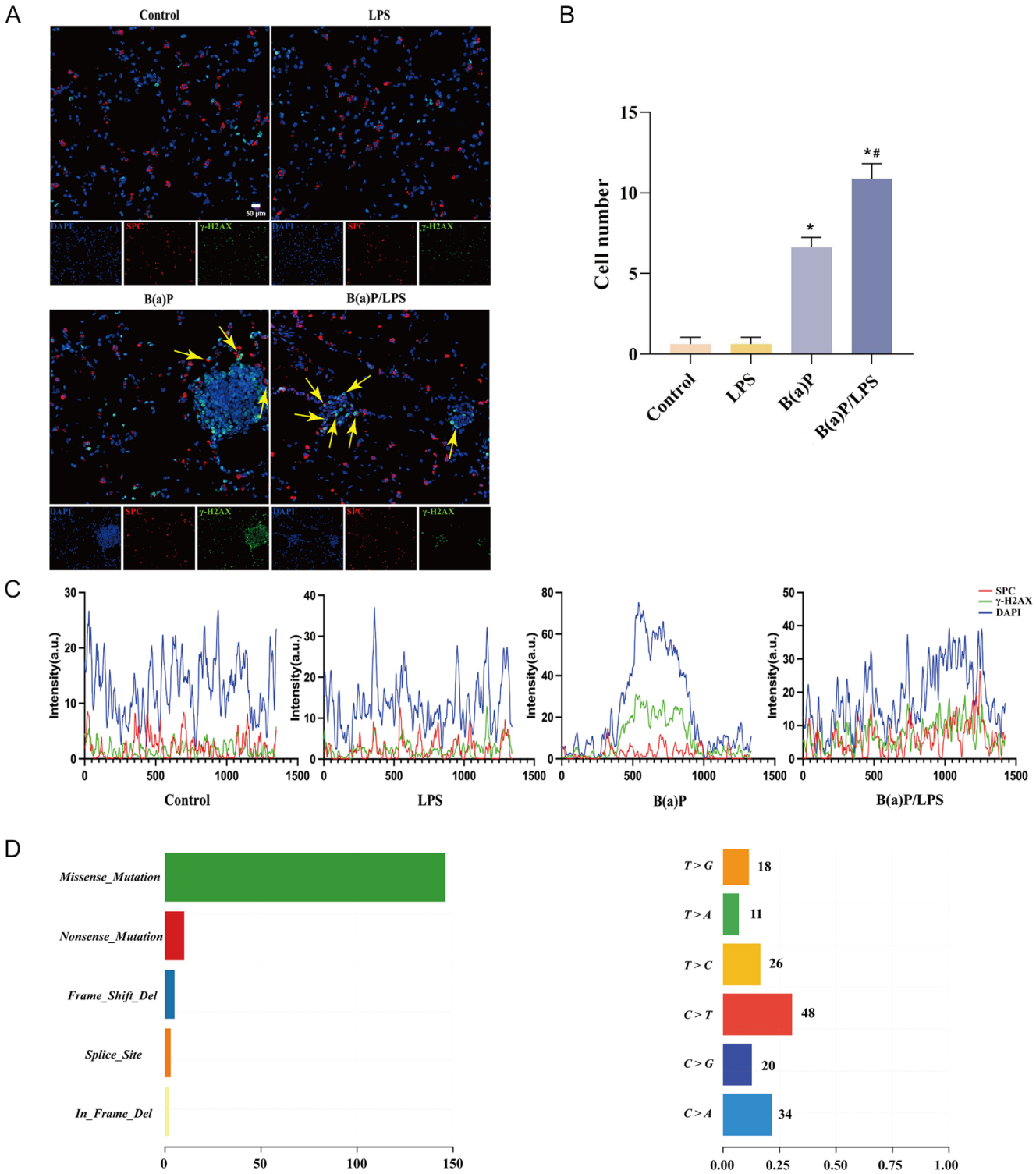

Figure 4. DNA damage and genetic mutations of AT2 cells in inflammation-related lung tumorigenesis (A–C) Immunofluorescence double staining, immunofluorescence co-localization, and cell counting analysis of the AT2 cell marker SPC and DNA damage marker γ-H2AX. SPC is a cytoplasmic protein labeled with red fluorescence, γ-H2AX is a nuclear protein labeled with green fluorescence, and DAPI is a nuclear stain labeled with blue fluorescence (scale bar: 50 μm). (D) The types of DNA mutations in AT2 cells and the number of single nucleotide variations within each mutation category.

whole lung was decreased in the B(a)P/LPS group, we inferred that most AT2 cells cannot proliferate or be repaired by B(a)P/LPS.

Genetic damage and gene mutations are the fundamental causes of tumorigenesis. The expression of the DNA damage protein γ-

Table 2. Tumor-associated genes with mutations occurring in the B(a)P group

Gene	Variant classification	Variant type	Reference allele	Tumor Seq allele
Api5	Missense mutation	SNP	A	T
Atg2a	Nonsense mutation	SNP	G	T
Stard13	Missense mutation	SNP	A	G
Col3al	Missense mutation	SNP	G	A
Itga10	Missense mutation	SNP	C	G
Yrdc	Missense mutation	SNP	G	A
Zbtb8b	Frame shift Del	NA	AAGTTGGGCCG	–
Siglecf	Missense mutation	SNP	G	C
Sun2	Missense mutation	SNP	C	A
Abca3	Missense mutation	SNP	T	G
Cul7	Missense mutation	SNP	G	T
Nxf1	Missense mutation	SNP	C	G

Table 3. Tumor-associated genes with mutations occurring in the B(a)P/LPS group

Gene	Variant classification	Variant type	Reference allele	Tumor Seq allele
Rasal3	Frame shift Del	NA	GTTTCATGTATTCATCAAT	–
Tnfsf14	Missense mutation	SNP	G	A
Map3k4	Missense mutation	SNP	A	C
Habp2	Missense mutation	SNP	C	G
Scarf2	Missense mutation	SNP	A	G
Dnajc22	Nonsense mutation	SNP	G	A
Vcan	Missense mutation	SNP	C	A
Sema4d	Nonsense mutation	SNP	C	A
Unc79	Missense mutation	SNP	C	A
Col6a6	Missense mutation	SNP	C	T
Fgl1	Missense mutation	SNP	A	C
Ptdss2	Missense mutation	SNP	C	T
Padi6	Missense mutation	SNP	T	C
Usp1	Missense mutation	SNP	G	A
Lgsf1	Missense mutation	SNP	C	T
Sema6c	Missense mutation	SNP	C	A

H2AX (a marker of DNA double-strand breaks) in AT2 cells was increased in lung cancer tissue in both the B(a)P and B(a)P/LPS groups, and the γ-H2AX level in AT2 cells from mice exposed to B(a)P/LPS was greater than that in AT2 cells from the B(a)P group. It is inferred that chronic inflammation can induce the activation of free radicals to aggravate them [37,38]. Furthermore, persistent and unrepaired DNA damage significantly increases the risk of gene mutations [39]; when gene damage results in the mutation of oncogenes or tumor suppressor genes, tumors develop [40,41]. In this study, DNA whole-exome sequencing of AT2 cells sorted from whole-lung tissue revealed 16 cancer-related gene mutations in the B(a)P/LPS group (including mutations in oncogenes *Vcan* and *Sema4d* and tumor suppressor genes *Rasal3* and *Map3k4*), which was greater than the 12 cancer-related gene mutations in the B(a)P group with no mutations in these genes. We inferred that the LPS-induced chronic inflammatory microenvironment may generate excessive free radicals, impair DNA repair mechanisms, and cause DNA damage, which triggers genetic mutations in AT2 cells, ultimately driving inflammation-related lung tumorigenesis.

Autophagy is closely related to carcinogenesis. In this study, we performed single-cell RNA transcriptomics and screened out the autophagy-related genes Foxo3 and Ppp2r5a, which are enriched in the PI3K-Akt signaling pathway, and verified the downregulation of the autophagy-related genes *Foxo3*, *Ppp2r5a*, *Lc3b* and *Atg5* in AT2 cells in the B(a)P/LPS group compared with those in the B(a)P group. Ppp2r5a is a key negative regulator of the Akt signaling pathway. When Ppp2r5a is downregulated, the Akt signaling pathway is activated, and the upregulation of phosphorylated Akt inhibits the translocation of Foxo3 from the cytoplasm to the nucleus. Inactivation of Foxo3 can suppress the formation and maturation of autophagosomes [42,43]. Finally, the expression of autophagy-related genes decreases, and autophagy is inhibited. Studies have shown that LPS activates the TLR4 pathway in pulmonary epithelial cells, leading to mTOR activation and a subsequent reduction in the expression of autophagy markers in LPS-induced acute lung injury [44]. Similarly, the PI3K-Akt-mTOR

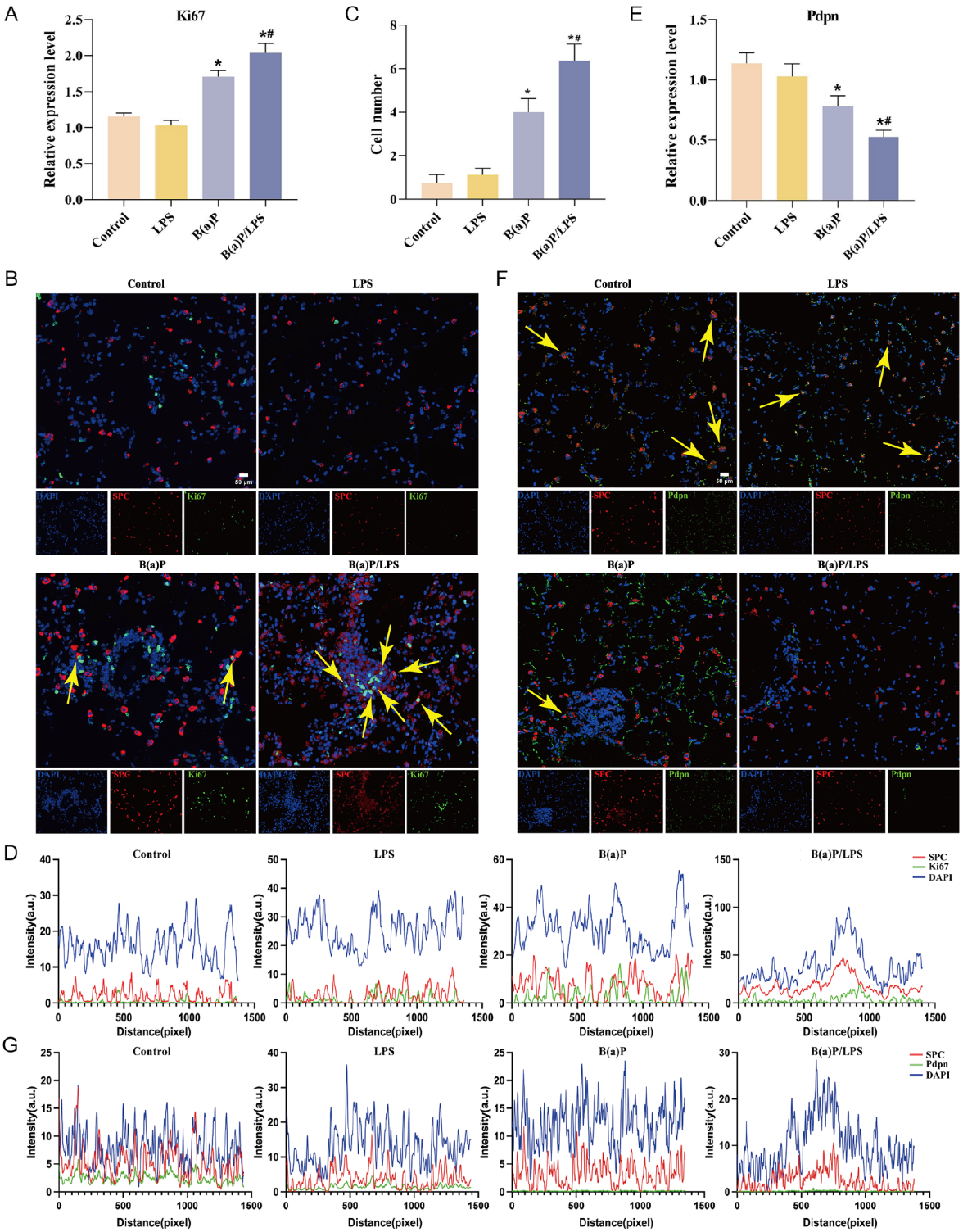

Figure 5. Functional abnormalities of AT2 cells in mice with inflammation-related lung tumorigenesis (A) The relative expression level of the proliferation marker gene Ki67 in AT2 cells. (B–D) Cell counting analysis, immunofluorescence double staining and immunofluorescence co-localization of the AT2 cell marker SPC and the proliferation marker protein Ki67. SPC is a cytoplasmic protein labeled with red fluorescence, Ki67 is a nuclear protein labeled with green fluorescence, and DAPI is a nuclear stain labeled with blue fluorescence (scale bar: 50 μm). (E) The relative expression level of the differentiation marker gene *Pdpn* in AT2 cells. (F,G) Immunofluorescence double staining and immunofluorescence co-localization of the AT2 cell marker SPC and the differentiation marker protein Pdpn. SPC is a cytoplasmic protein labeled with red fluorescence, Pdpn is the protein marker of AT1 cell labeled with green fluorescence, and DAPI is a nuclear stain labeled with blue fluorescence (scale bar: 50 μm). $^{*}P < 0.05$ vs Control; $^{\#}P < 0.05$ vs B(a)P.

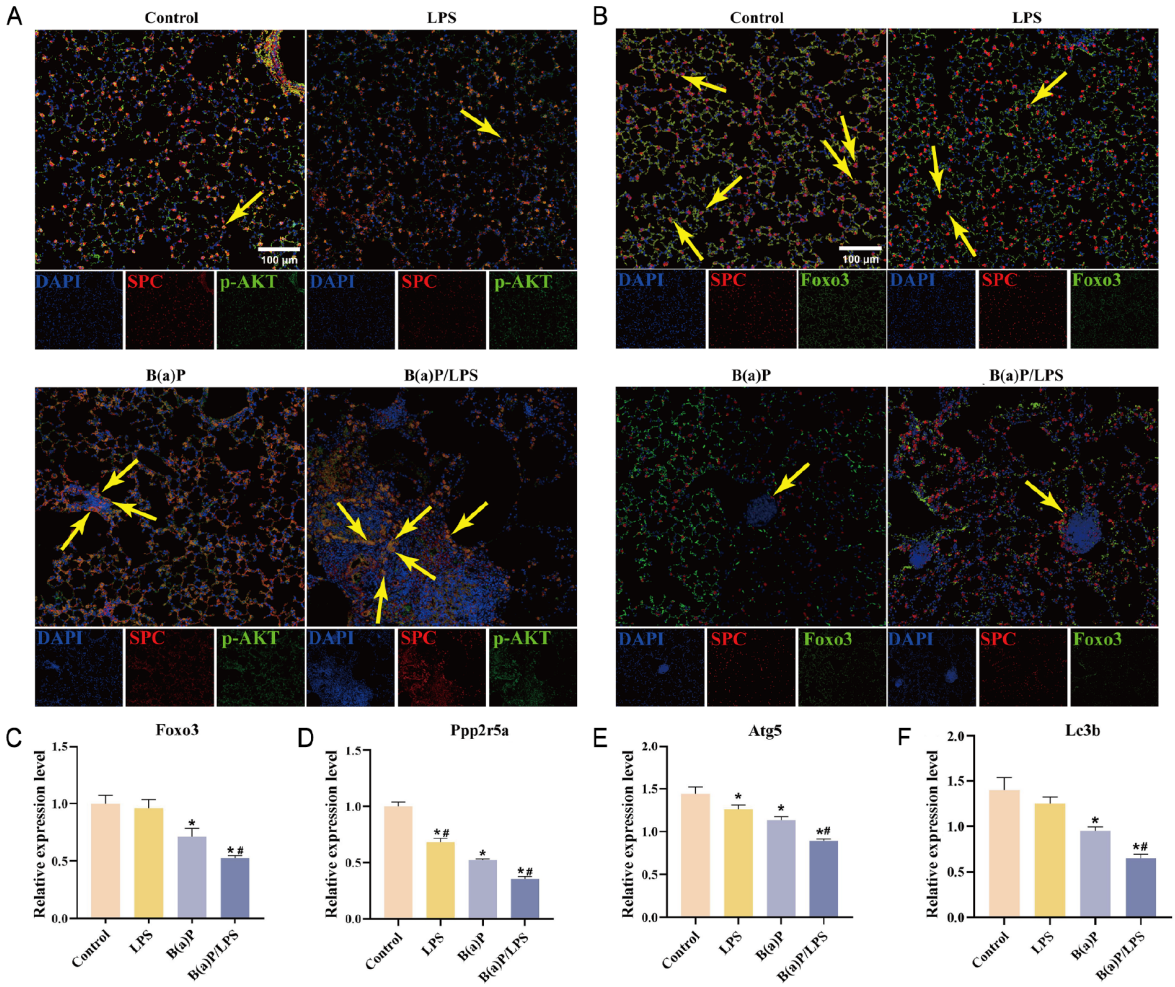

Figure 6. Autophagy of AT2 cells is reduced in mice with inflammation-related lung tumorigenesis (A) Immunofluorescence double staining of p-Akt in AT2 cells. SPC is a cytoplasmic protein labeled with red fluorescence, p-Akt is labeled with green fluorescence, and DAPI is a nuclear stain labeled with blue fluorescence (scale bar: 100 μm). (B) Immunofluorescence double staining of Foxo3 in AT2 cells. SPC is a cytoplasmic protein labeled with red fluorescence, Foxo3 is labeled with green fluorescence, and DAPI is a nuclear stain labeled with blue fluorescence (scale bar: 100 μm). (C,D) The relative expression levels of the gene *Ppp2r5a* and *Foxo3* in AT2 cells. $^{*}P < 0.05$ vs Control; $^{\#}P < 0.05$ vs B(a)P. (E,F) The relative expression levels of the autophagy marker genes *Lc3b* and *Atg5* in AT2 cells. *Atg5* is a marker gene for the early stage of autophagosome formation. *Lc3b* is a marker gene for autophagosome maturation. $^{*}P < 0.05$ vs Control; $^{\#}P < 0.05$ vs B(a)P.

pathway can be activated by LPS to inhibit autophagy [45]. In addition to these mechanisms, the inflammatory microenvironment induced by LPS may reduce autophagy in AT2 cells. A possible explanation for this finding may be the presence of inflammatory cytokines [46,47]. A previous study by our research group revealed that in the lung cancer tissue of mice exposed to B(a)P and LPS, the NLRP3 inflammasome was activated, and the inflammatory cytokines IL-18 and IL-1β were significantly increased compared with those in mice exposed to B(a)P alone [48]. Studies have revealed that IL-18 [49] and IL-1β [47] can suppress autophagy.

Dysregulation of autophagy can contribute to genomic instability and the accumulation of DNA damage through multiple mechanisms. Studies have shown that the loss of key autophagy genes, such as *Atg5* or *Atg7*, leads to the accumulation of damaged mitochondria, which are major sources of reactive oxygen species (ROS). Excessive ROS production can directly attack DNA, resulting in strand breaks and subsequent accumulation of DNA damage. Similarly, impaired autophagy causes the accumulation of the autophagy adaptor protein p62, which aberrantly activates NRF2 and indirectly promotes the survival and proliferation of damaged cells, thereby exacerbating genomic instability and tumorigenesis [50,51]. Therefore, autophagy dysregulation represents a key mechanism underlying the accumulation of DNA damage during lung carcinogenesis. In addition, autophagy can regulate cell proliferation and differentiation. In this study, decreased autophagy might be related to accelerated proliferation and impaired differentiation of AT2 cells in lung cancer tissue. Many examples support this viewpoint: the inhibition of autophagy promotes the proliferation of hepatocellular carcinoma [52] and mammary epithelial cells [53]. Furthermore, silencing the autophagy-related gene *Atg5* reduces the differentiation of ovarian granulosa cells [54], and the inhibition of autophagy significantly impairs osteoclast differentiation [55]. Therefore, in this study, LPS-mediated chronic inflammation reduced autophagy in AT2 cells, and the decreased autophagy of malignantly transformed AT2 cells in lung cancer tissue may be an important reason for the increased incidence of lung cancer in the B

(a)P/LPS group, possibly through increased proliferation of abnormal AT2 cells and inhibited differentiation of AT2 cells for repair.

We acknowledge that these are limitations to the present study. Owing to sample size, single-cell RNA sequencing and DNA whole-exome sequencing were unable to perform sequencing specifically on tumor sites, and whole-lung tissue sequencing was conducted instead. While enabling the detection of alterations across various cell types throughout the lung (including AT2 cells), these methods highlight the need for future optimization to achieve site-specific tumor profiling.

In conclusion, in inflammation-related lung tumorigenesis, LPS-induced chronic inflammation increases the number of gene mutations in AT2 cells, increases the levels of DNA damage and proliferation markers, decreases the levels of differentiation markers in AT2 cells, and decreases the level of autophagy in AT2 cells in lung cancer tissue, which may be an important mechanism for increased inflammation-related lung tumorigenesis. To our knowledge, these are the first studies to explore the genetic mutation and dysfunction of AT2 stem cells, the origin cells of LUAD, and elucidate the mechanism of autophagy in inflammation-related lung tumorigenesis. These findings further reveal the inflammatory microenvironment and lung carcinogenesis, and increasing autophagy in malignantly transformed AT2 cells via chemical activators may be a novel therapeutic approach to prevent carcinogen-induced lung cancer, especially inflammation-related lung tumorigenesis.

Supplementary Data

Supplementary data are available at *Acta Biochimica et Biophysica Sinica* online.

Data Availability

Data can be accessed upon reasonable request from the corresponding authors.

Acknowledgement

We appreciate all the participants and support from the Henan Key Laboratory of Tumor Epidemiology in this study.

Funding

This work was supported by the grants from the Chief Scientist Innovation Project from China National Tobacco Corporation (No. 322022CK0480), the grant from Beijing Life Science Academy (BLSA:2024400CC0040), and the Henan Provincial Center for Disease Control and Prevention Science and Technology Research Special Project (No. HNCDCZD20250201).

Conflict of Interest

The authors declare that they have no conflict of interest.

References

1. Lin Y, Xu H, Wang K, Wang X, Wu X, Tang Z, Lin Y, *et al.* Transcriptomics integrated with metabolomics reveals the effect of benzo[a]pyrene exposure on acute lung injury. *Ecotoxicol Environ Saf* 2024, 288: 117323
2. Bull S, Collins C. Promoting the use of BaP as a marker for PAH exposure in UK soils. *Environ Geochem Health* 2013, 35: 101–109
3. Zhang Y, Yang Y, Chen W, Mi C, Xu X, Shen Y, Zheng Z, *et al.* BaP/BPDE suppressed endothelial cell angiogenesis to induce miscarriage by promoting MARCHF1/GPX4-mediated ferroptosis. *Environ Int* 2023, 180: 108237
4. Liu Y, Zhang H, Zhang H, Niu Y, Fu Y, Nie J, Yang A, *et al.* Mediation effect of AhR expression between polycyclic aromatic hydrocarbons exposure and oxidative DNA damage among Chinese occupational workers. *Environ Pollution* 2018, 243: 972–977
5. Armstrong BG, Gibbs G. Exposure–response relationship between lung cancer and polycyclic aromatic hydrocarbons (PAHs). *Occup Environ Med* 2009, 66: 740–746
6. Ryu JK, Kim SJ, Rah SH, Kang JI, Jung HE, Lee D, Lee HK, *et al.* Reconstruction of LPS transfer cascade reveals structural determinants within LBP, CD14, and TLR4-MD2 for efficient LPS recognition and transfer. *Immunity* 2017, 46: 38–50
7. Wang Q, Liu S. The effects and pathogenesis of PM2.5 and its components on chronic obstructive pulmonary disease. *Int J Chron Obstruct Pulmon Dis* 2023, 18: 493–506
8. Yang J, Kim EK, Park HJ, McDowell A, Kim YK. The impact of bacteria-derived ultrafine dust particles on pulmonary diseases. *Exp Mol Med* 2020, 52: 338–347
9. Yamashita M, Niisato M, Kawasaki Y, Karaman S, Robciuc MR, Shibata Y, Ishida Y, *et al.* VEGF-C/VEGFR-3 signalling in macrophages ameliorates acute lung injury. *Eur Respir J* 2022, 59: 2100880
10. Bray F, Laversanne M, Sung H, Ferlay J, Siegel RL, Soerjomataram I, Jemal A. Global cancer statistics 2022: GLOBOCAN estimates of incidence and mortality worldwide for 36 cancers in 185 countries. *CA Cancer J Clin* 2024, 74: 229–263
11. Liang J, Bi G, Huang Y, Zhao G, Sui Q, Zhang H, Bian Y, *et al.* MAFF confers vulnerability to cisplatin-based and ionizing radiation treatments by modulating ferroptosis and cell cycle progression in lung adenocarcinoma. *Drug Resist Updat* 2024, 73: 101057
12. He Q, Qu M, Xu C, Wu L, Xu Y, Su J, Bao H, *et al.* Smoking-induced CCNA2 expression promotes lung adenocarcinoma tumorigenesis by boosting AT2/AT2-like cell differentiation. *Cancer Lett* 2024, 592: 216922
13. Xu ZY, Brown L, Pan GW, Li G, Feng YP, Guan DX, Liu TF, *et al.* Lifestyle, environmental pollution and lung cancer in cities of Liaoning in northeastern China. *Lung Cancer* 1996, 14: S149–S160
14. Gharibvand L, Lawrence Beeson W, Shavlik D, Knutsen R, Ghamsary M, Soret S, Knutsen SF. The association between ambient fine particulate matter and incident adenocarcinoma subtype of lung cancer. *Environ Health* 2017, 16: 71
15. Molina JR, Yang P, Cassivi SD, Schild SE, Adjei AA. Non-small cell lung cancer: epidemiology, risk factors, treatment, and survivorship. *Mayo Clinic Proc* 2008, 83: 584–594
16. Lee G, Walser TC, Dubinett SM. Chronic inflammation, chronic obstructive pulmonary disease, and lung cancer. *Curr Opin Pulmonary Med* 2009, 15: 303–307
17. Huang L, Duan S, Shao H, Zhang A, Chen S, Zhang P, Wang N, *et al.* NLRP3 deletion inhibits inflammation-driven mouse lung tumorigenesis induced by benzo(a)pyrene and lipopolysaccharide. *Respir Res* 2019, 20: 20
18. Naranjo S, Cabana CM, LaFave LM, Romero R, Shanahan SL, Bhutkar A, Westcott PMK, *et al.* Modeling diverse genetic subtypes of lung adenocarcinoma with a next-generation alveolar type 2 organoid platform. *Genes Dev* 2022, 36: 936–949
19. Sainz de Aja J, Dost AFM, Kim CF. Alveolar progenitor cells and the origin of lung cancer. *J Intern Med* 2021, 289: 629–635
20. Li Z, Zhuang X, Pan CH, Yan Y, Thummalapalli R, Hallin J, Torborg S, *et al.* Alveolar differentiation drives resistance to *KRAS* inhibition in lung adenocarcinoma. *Cancer Discov* 2024, 14: 308–325
21. Boo HJ, Min HY, Park CS, Park JS, Jeong JY, Lee SY, Kim WY, *et al.* Dual

impact of IGF2 on alveolar stem cell function during tobacco-induced injury repair and development of pulmonary emphysema and cancer. *Cancer Res* 2023, 83: 1782–1799
22. Li X, He S, Ma B. Autophagy and autophagy-related proteins in cancer. *Mol Cancer* 2020, 19: 12
23. Liu SZ, Yao SJ, Yang H, Liu SJ, Wang YJ. Autophagy: regulator of cell death. *Cell Death Dis* 2023, 14: 648
24. Sun Y, Shen W, Hu S, Lyu Q, Wang Q, Wei T, Zhu W, ***et al.*** METTL3 promotes chemoresistance in small cell lung cancer by inducing mitophagy. *J Exp Clin Cancer Res* 2023, 42: 65
25. Saitoh T, Fujita N, Jang MH, Uematsu S, Yang BG, Satoh T, Omori H, ***et al.*** Loss of the autophagy protein Atg16L1 enhances endotoxin-induced IL-1β production. *Nature* 2008, 456: 264–268
26. Yang S, Li F, Lu S, Ren L, Bian S, Liu M, Zhao D, ***et al.*** Ginseng root extract attenuates inflammation by inhibiting the MAPK/NF-κB signaling pathway and activating autophagy and p62-Nrf2-Keap1 signaling *in vitro* and *in vivo*. *J EthnoPharmacol* 2022, 283: 114739
27. Gui X, Yang H, Li T, Tan X, Shi P, Li M, Du F, ***et al.*** Autophagy induction via STING trafficking is a primordial function of the cGAS pathway. *Nature* 2019, 567: 262–266
28. Racanelli AC, Kikkers SA, Choi AMK, Cloonan SM. Autophagy and inflammation in chronic respiratory disease. *Autophagy* 2018, 14: 221–232
29. Katzen J, Beers MF. Contributions of alveolar epithelial cell quality control to pulmonary fibrosis. *J Clin Invest* 2020, 130: 5088–5099
30. Huang L, Zhang P, Duan S, Shao H, Gao M, Zhang Q, Feng F. The comparison of two mouse models of inflammation-related lung tumorigenesis induced by benzo(a)pyrene and lipopolysaccharide. *Exp Anim* 2019, 68: 301–306
31. Wu T, Hu E, Xu S, Chen M, Guo P, Dai Z, Feng T, ***et al.*** ClusterProfiler 4.0: a universal enrichment tool for interpreting omics data. *Innovation* 2021, 2: 100141
32. Yu G, Wang LG, Yan GR, He QY. DOSE: an R/Bioconductor package for disease ontology semantic and enrichment analysis. *Bioinformatics* 2015, 31: 608–609
33. Gu Z, Eils R, Schlesner M. Complex heatmaps reveal patterns and correlations in multidimensional genomic data. *Bioinformatics* 2016, 32: 2847–2849
34. García Campelo MR, Curbera GA, Gallego GA, Pulido EG, Antón Aparicio LM. Stem cell and lung cancer development: blaming the Wnt, Hh and Notch signalling pathway. *Clin Transl Oncol* 2011, 13: 77–83
35. He G, Karin M. NF-κB and STAT3-key players in liver inflammation and cancer. *Cell Res* 2011, 21: 159–168
36. Coussens LM, Werb Z. Inflammation and cancer. *Nature* 2002, 420: 860–867
37. Jomova K, Raptova R, Alomar SY, Alwasel SH, Nepovimova E, Kuca K, Valko M. Reactive oxygen species, toxicity, oxidative stress, and antioxidants: chronic diseases and aging. *Arch Toxicol* 2023, 97: 2499–2574
38. Huang R, Zhou PK. DNA damage repair: historical perspectives, mechanistic pathways and clinical translation for targeted cancer therapy. *Sig Transduct Target Ther* 2021, 6: 254
39. Kawanishi S, Ohnishi S, Ma N, Hiraku Y, Murata M. Crosstalk between DNA damage and inflammation in the multiple steps of carcinogenesis. *Int J Mol Sci* 2017, 18: 1808
40. Napoli M, Wu SJ, Gore BL, Abbas HA, Lee K, Checker R, Dhar S, ***et al.*** ΔNp63 regulates a common landscape of enhancer associated genes in non-small cell lung cancer. *Nat Commun* 2022, 13: 614
41. Zuo W, Rostami MR, Shenoy SA, LeBlanc MG, Salit J, Strulovici-Barel Y, O'Beirne SL, ***et al.*** Cell-specific expression of lung disease risk-related genes in the human small airway epithelium. *Respir Res* 2020, 21: 200
42. Niu J, Yan T, Guo W, Wang W, Ren T, Huang Y, Zhao Z, ***et al.*** The COPS3-FOXO3 positive feedback loop regulates autophagy to promote cisplatin resistance in osteosarcoma. *Autophagy* 2023, 19: 1693–1710
43. Yan D, Yang Y, Lang J, Wang X, Huang Y, Meng J, Wu J, ***et al.*** SIRT1/FOXO3-mediated autophagy signaling involved in manganese-induced neuroinflammation in microglia. *Ecotoxicol Environ Saf* 2023, 256: 114872
44. Hu Y, Lou J, Mao YY, Lai TW, Liu LY, Zhu C, Zhang C, ***et al.*** Activation of MTOR in pulmonary epithelium promotes LPS-induced acute lung injury. *Autophagy* 2016, 12: 2286–2299
45. Xie T, Xu Q, Wan H, Xing S, Shang C, Gao Y, He Z. Lipopolysaccharide promotes lung fibroblast proliferation through autophagy inhibition via activation of the PI3K-Akt-mTOR pathway. *Lab Invest* 2019, 99: 625–633
46. Biasizzo M, Kopitar-Jerala N. Interplay between NLRP3 inflammasome and autophagy. *Front Immunol* 2020, 11: 591803
47. Meyers AK, Wang Z, Han W, Zhao Q, Zabalawi M, Duan L, Liu J, ***et al.*** Pyruvate dehydrogenase kinase supports macrophage NLRP3 inflammasome activation during acute inflammation. *Cell Rep* 2023, 42: 111941
48. Gao M, Zhang P, Huang L, Shao H, Duan S, Li C, Zhang Q, ***et al.*** Is NLRP3 or NLRP6 inflammasome activation associated with inflammation-related lung tumorigenesis induced by benzo(a)pyrene and lipopolysaccharide? *Ecotoxicol Environ Saf* 2019, 185: 109687
49. Salminen A, Kaarniranta K, Kauppinen A. Inflammaging: disturbed interplay between autophagy and inflammasomes. *Aging* 2012, 4: 166–175
50. Chen S, Guan JL. Tumor-promoting and -suppressive roles of autophagy in the same mouse model of *Braf* V600E-driven lung cancer. *Cancer Discov* 2013, 3: 1225–1227
51. Rao S, Tortola L, Perlot T, Wirnsberger G, Novatchkova M, Nitsch R, Sykacek P, ***et al.*** A dual role for autophagy in a murine model of lung cancer. *Nat Commun* 2014, 5: 3056
52. Desideri E, Castelli S, Dorard C, Toifl S, Grazi GL, Ciriolo MR, Baccarini M. Impaired degradation of YAP1 and IL6ST by chaperone-mediated autophagy promotes proliferation and migration of normal and hepatocellular carcinoma cells. *Autophagy* 2023, 19: 152–162
53. Qu X, Yu J, Bhagat G, Furuya N, Hibshoosh H, Troxel A, Rosen J, ***et al.*** Promotion of tumorigenesis by heterozygous disruption of the beclin 1 autophagy gene. *J Clin Invest* 2003, 112: 1809–1820
54. Shao T, Ke H, Liu R, Xu L, Han S, Zhang X, Dang Y, ***et al.*** Autophagy regulates differentiation of ovarian granulosa cells through degradation of WT1. *Autophagy* 2022, 18: 1864–1878
55. Zhao Y, Chen G, Zhang W, Xu N, Zhu J, Jia J, Sun Z, ***et al.*** Autophagy regulates hypoxia-induced osteoclastogenesis through the HIF-1α/BNIP3 signaling pathway. *J Cell Physiol* 2012, 227: 639–648